Moving through the Phase Diagram: Morphology Formation in Solution Cast Polymer–Fullerene Blend Films for Organic Solar Cells

Benjamin Schmidt-Hansberg,[†,*] Monamie Sanyal,[‡] Michael F. G. Klein,[§] Marina Pfaff,[⊥] Natalie Schnabel,[†] Stefan Jaiser,[†] Alexei Vorobiev,[¶] Erich Müller,[⊥] Alexander Colsmann,[§] Philip Scharfer,[†] Dagmar Gerthsen,[⊥] Uli Lemmer,[§] Esther Barrena,[‡,#,*] and Wilhelm Schabel[†]

[†]Thermal Process Engineering, Thin Film Technology, Karlsruhe Institute of Technology (KIT), Kaiserstraße 12, D-76131 Karlsruhe, Germany, [‡]Max Planck Institute for Metals Research, Heisenbergstrasse 3, 70569 Stuttgart, Germany, [§]Light Technology Institute, Karlsruhe Institute of Technology (KIT), Kaiserstraße 12, D-76131 Karlsruhe, Germany, [⊥]Laboratory for Electron Microscopy and Center for Functional Nanostructures (CFN), Karlsruhe Institute of Technology (KIT), Kaiserstraße 12, D-76131 Karlsruhe, Germany, [¶]European Synchrotron Radiation Facility BP 220, 38043 Grenoble Cedex 9, France, and [#]Institut de Ciència de Materials de Barcelona (ICMAB-CSIC), 08193 Bellaterra, Spain

ABSTRACT The efficiency of organic bulk heterojunction solar cells strongly depends on the multiscale morphology of the interpenetrating polymer–fullerene network. Understanding the molecular assembly and the identification of influencing parameters is essential for a systematic optimization of such devices. Here, we investigate the molecular ordering during the drying of doctor-bladed polymer–fullerene blends on PEDOT:PSS-coated substrates simultaneously using *in situ* grazing incidence X-ray diffraction (GIXD) and laser reflectometry. In the process of blend crystallization, we observe the nucleation of well-aligned P3HT crystallites in edge-on orientation at the interface at the instant when P3HT solubility is crossed. A comparison of the real-time GIXD study at ternary blends with the binary phase diagrams of the drying blend film gives evidence of strong polymer–fullerene interactions that impede the crystal growth of PCBM, resulting in the aggregation of PCBM in the final drying stage. A systematic dependence of the film roughness on the drying time after crossing P3HT solubility has been shown. The highest efficiencies have been observed for slow drying at low temperatures which showed the strongest P3HT interchain π–π-ordering along the substrate surface. By adding the "unfriendly" solvent cyclohexanone to a chlorobenzene solution of P3HT:PCBM, the solubility can be crossed prior to the drying process. Such solutions exhibit randomly orientated crystalline structures in the freshly cast film which results in a large crystalline orientation distribution in the dry film that has been shown to be beneficial for solar cell performance.

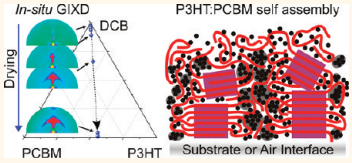

KEYWORDS: self-assembly · *in situ* grazing incidence X-ray diffraction (GIXD) · solubility · drying kinetics · doctor blade · P3HT:PCBM · solvent mixture

Bulk heterojunction (BHJ) solar cells from organic/polymer semiconductors are a promising technology for low cost and large area photovoltaic devices on rigid or flexible substrates.[1,2] For organic photovoltaics (OPV), the BHJ nanomorphology is a key factor in the optimization of solar cell efficiencies.[3−5] Usually, organic BHJ solar cells comprise a blend of electron-donating, semiconducting polymer and electron-accepting fullerene, forming an interpenetrating polymer–fullerene network, as the photoactive layer. The length scale of the polymer–fullerene phase segregation should be in the range of 5–10 nm, which is the exciton diffusion length,[6−8] to enable efficient charge separation at the polymer–fullerene interface. The subsequent charge transport requires continuous percolation paths to the electrodes.[9] This process is enhanced by high charge carrier mobility within the polymer and fullerene phase, which has been shown to be supported by high crystalline orientation in the direction of charge carrier conductance.[10]

Hence, it is of great interest to control the film morphology, which evolves during solvent evaporation (film drying) of the BHJ layer. The drying process offers easily controllable parameters, such as the rate of solvent evaporation[11−13] (drying gas velocity, ambient solvent vapor pressure) and the temperature.[14,15] These parameters allow for tuning the assembling time and for changing the solubility which influences solubility driven mechanisms[16] such as gelation[17,18] and crystallization.[19] For example, changes in the evaporation rate controlled through the nitrogen air flow influence the retention time in different regions of the phase diagram. Because of the high diffusional mobility of the dissolved organic semiconductors in the wet film, the drying step allows for molecular diffusion and ordering over large distances. This process is fundamentally different from postdrying treatments where dry films are

* Address correspondence to schmidt-hansberg@kit.edu, ebarrena@icmab.es.

Received for review May 27, 2011 and accepted October 16, 2011.

Published online October 16, 2011
10.1021/nn2036279

treated by temperature[20−24] or solvent annealing.[25−27] The drying process offers additional routes for tailoring the film structure in comparison to postdrying treatments which provide less mobility, but stronger interactions between the densely packed solid compounds.

So far, the dynamics of polymer−fullerene self-assembly mechanisms during film formation have not been investigated extensively. However, knowledge of the driving mechanisms for self-assembly is of crucial importance in order to optimize fabrication methods and design new materials with improved properties.

This work investigates the dynamics and thermodynamics of molecular ordering during film drying. For this study we choose the established material system poly-(3-hexylthiophene-2,5-diyl) (P3HT), [6,6]-phenyl C_{61}-butyric acid methyl ester (PCBM) and 1,2-dichlorobenzene (DCB). Since crystallization is a solubility driven mechanism, phase diagrams of P3HT and PCBM solutions have been determined. The pathway through the phase diagram is compared with the structural evolution of the ternary blend as observed in real time by GIXD. Additionally, the influence of drying process parameters on the multiscale film morphology and optoelectronic solar cell device properties have been investigated *ex situ* by atomic force microscopy (AFM) and scanning transmission electron microscopy (STEM).[28] Finally, the effect of altering the phase behavior by addition of an "unfriendly" solvent to a "friendly" solvent has been investigated *in situ* during film formation for P3HT:PCBM doctor-bladed from a solvent mixture of chlorobenzene−cyclohexanone (CB:CHN).

With a detailed discussion of the time-resolved structural evolution in conjunction with the impact of drying conditions on final film morphology, we provide a fundamental understanding of morphology formation in BHJ layers and design rules for the drying process.

RESULTS AND DISCUSSION

Binary Phase Diagrams of P3HT and PCBM Solutions. So far, the P3HT:PCBM phase diagram is only known for crystallization from melt of the binary blend measured by calorimetry[29,30] and dynamic mechanical analysis.[31] Literature available on P3HT and PCBM solubility in DCB is limited to a few reports at room temperature.[32,33] Here we determine the phase diagrams of the binary systems P3HT-DCB and PCBM-DCB by preparing a slightly oversaturated solution state, whereupon, in a subsequent step after centrifugation, the concentration in the coexisting phases was determined with a refractometer for different temperatures (see Experimental Methods section for more details).

Figure 1b depicts the composition of the two coexisting phases of a P3HT solution in DCB for each

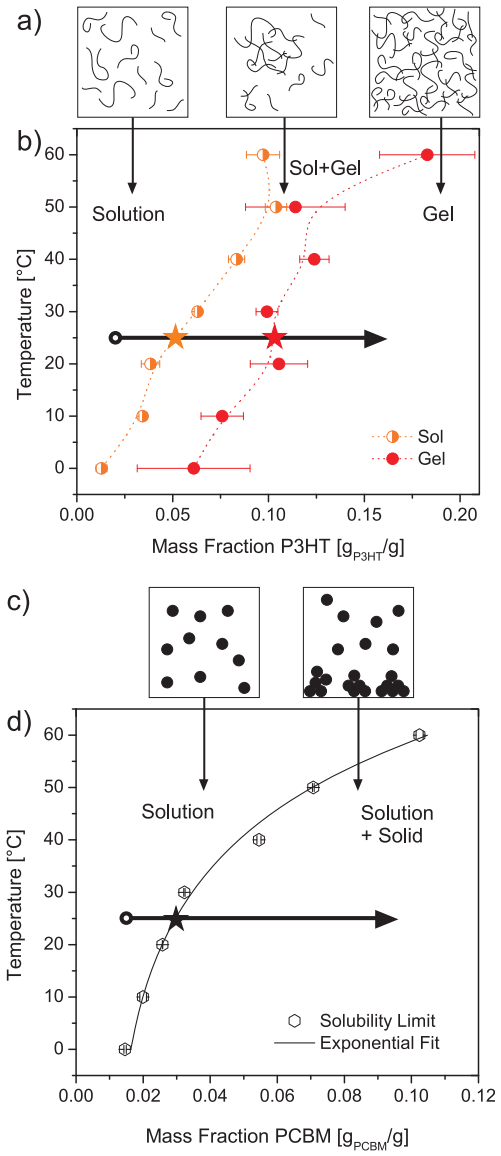

Figure 1. Binary phase diagram of P3HT and PCBM solutions in DCB. (a) Schematic of the transition from solution to gel-state with polymer aggregation in the unstable two-phase region, before the solution turns into a higher viscous gel during solvent evaporation. (b) Phase diagram of P3HT-DCB solution with unstable two-phase region between the solution and gel state. Dashed lines are a guide to the eyes. (c) Schematic of fullerene aggregation after crossing the solubility limit. (d) Solubility of PCBM in DCB as a function of temperature. The arrows indicate the drying process at 25 °C, and the star symbols represent the instant of phase transition.

temperature at thermodynamic equilibrium, namely, the solid-poor sol phase (half-filled circles) and the solid-rich gel phase (filled circles). These two states form the binodal curve which surrounds the thermodynamically unstable two-phase region. If the solution or film composition is situated in this unstable region it tends to phase separate as schematically shown in Figure 1a.[34,35] The solution is stable for concentrations below 40 mg/mL ($x_s < 3$ wt %; $x_s = m_{solid}/(m_{DCB} + m_{solid})$) as usually used for the coating of such solutions for organic solar cells at room temperature. With solvent

evaporation at a constant temperature (arrow indicates evaporation at 25 °C), the P3HT solution reaches the solubility limit at a solid mass fraction of $x_s = 5.1$ wt % (interpolated for 25 °C) and enters the unstable binodal area. The demixing in this unstable area may be attributed to the strongly differing dynamics of the small solvent and comparatively big polymer molecules. As illustrated in Figure 1a, such a thermodynamically preferred demixing leads to an aggregation of polymer chains which are swollen with solvent and contain $x_s = 10.2$ wt % solid fraction. The residual sol phase contains 5.1 wt % solid fraction. Solid-rich aggregates start growing after the solution (the drying film) has entered the unstable area, until the whole film turns into the higher viscous gel phase. The width of the unstable two-phase region is almost zero at 50 °C (overlapping error bars) indicating an almost continuous increase of viscosity without phase separation at this drying temperature. Although gravity and density effects might not have an effect in such thin films of a few micrometers wet film thickness, it is noteworthy that the gel-phase (solid-rich) density is lower than the solution-phase (solid-poor) density due to the lower density of P3HT ($\rho_{P3HT} = 1.1$ g/mL) in comparison to DCB ($\rho_{DCB} = 1.3$ g/mL). Macroscopically, after centrifugation, this leads to a floating gel phase on top of the solution phase.

PCBM does not show a gelation behavior and exhibits a single solubility limit as depicted in Figure 1d which increases with temperature in contrast to P3HT. By crossing the solubility limit due to solvent evaporation, solid PCBM aggregates precipitate maintaining the residual solution at the solubility limit as shown schematically in Figure 1c. Depending on the evaporation kinetics of pure PCBM solution, this can lead to macroscopic crystals of several micrometers.[36]

***In-Situ* Observation of Structure Evolution.** Understanding structure formation in BHJ layers during solar cell fabrication requires an investigation of ternary polymer−fullerene−solvent (P3HT−PCBM−DCB) blends. Therefore, we compared the pathway through the superposition of the binary phase diagrams (Figure 1) with the evolution of crystallization of the ternary blend in thin films, studied *in situ* using GIXD and laser reflectometry simultaneously.

In the dedicated experimental setup (Figure 2a), two-dimensional (2D) GIXD diffraction patterns and film thicknesses were obtained immediately after doctor-blading the solution on a glass/PEDOT:PSS substrate. To increase the drying time, the wet film was dried at 25 °C without drying gas flow (drying accelerates with increasing gas flow velocity). The film composition (solvent mass fraction $x_{DCB} = m_{DCB}/(m_{DCB} + m_{solid})$ or solid mass fraction $x_s = 1 - x_{DCB}$) was obtained from the thickness measurement based on interference patterns by considering the changing optical and mass density and neglecting excess volume of the mixture.[15,37] Hence, it was possible to correlate the structural information derived from the X-ray diffraction analysis with the corresponding position in the phase diagram for each GIXD measurement. The position of each GIXD measurement is depicted in the ternary phase diagram (open circles in Figure 2c). The star symbols indicate the position of the binary solubility limits at the binary axis. Figure 2d shows the evolution of the (100) Bragg peak of P3HT during the course of film drying. P3HT has an edge-on configuration in this system (Figure 2b).[38−40] Initially, the P3HT Bragg peak has a spot-like shape which evolves into an often-reported wing-like shape during drying, suggesting that the mosaicity (angular orientation) of P3HT increases during drying as schematically shown in Figure 3d.[38−40]

The time evolution of the film composition obtained from laser reflectometry is plotted in Figure 3a. To study the entire evolution of the solvent fraction, a model of constant gas-phase mass transfer coefficient for the film drying kinetics was adapted to the experimental data.[15] Owing to the low solid fraction in highly diluted solutions, it has less influence on the solvent mass fraction initially. Therefore, the decrease of solvent mass fraction x_{DCB} proceeds slowly in the beginning. This leads to a long residence time at solvent fractions $x_{DCB} > 85$ wt %. As the solid fraction becomes significant, the solvent fraction x_{DCB} reduces rapidly, and a wide range of solvent fraction in the phase diagram is crossed quickly in a small window of drying time, offering little time for further molecular ordering (Figure 3a). Nevertheless, the thickness decreases almost linearly over the constant rate period (drying period I, marked in Figure 3a) due to an almost constant evaporation rate. This drying period is discussed in more detail elsewhere.[37] At high solid fractions (period II), the evaporation rate decreases due to the increased limitation of solvent diffusion (falling rate period). This is because the solvent is trapped in the film, providing less diffusional mobility for solvent transport to the surface. Thickness changes are very small in this period and cannot be resolved using reflectometry. Nevertheless the reflectometer signal changes until the optical properties remain constant, which allows for an experimental determination of the falling rate period. The state of settled optical properties is defined as "dry" although there might remain trace solvent in the film which can only be removed by thermal annealing.[41] The thickness evolution in this range can be resolved by ellipsometry.[42]

The bars in Figure 3a labeled with PCBM, P3HT (sol) and P3HT (gel) indicate the instants on the time scale when the solubility limits/phase transitions of each component are reached for the binary cases. The length of each bar originates from two cases of transferring the binary phase diagrams to the ternary system. As case i we assume that the solvent is

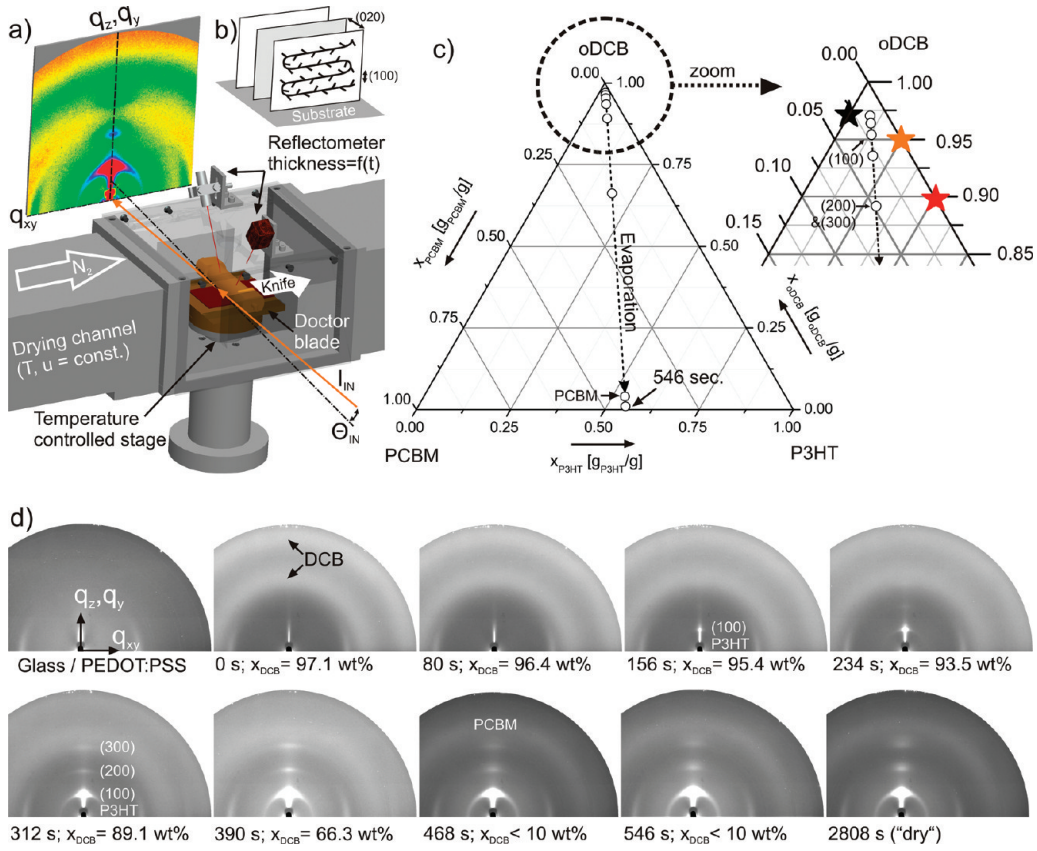

Figure 2. (a) Schematic of the experimental setup for simultaneous real time GIXD and laser reflectometry of doctor-bladed thin films in a controlled drying environment. (b) Schematic of P3HT unit cell. (c) Ternary phase diagram of P3HT–PCBM–DCB; the star symbols denote phase transitions in the binary cases. Each open circle symbol indicates a frame of GIXD measurements shown in panel d. While the first image is of PEDOT:PSS/glass substrate, the subsequent images show the evolution of film drying and crystallization. Below each image, the drying time and actual solvent fraction is mentioned.

distributed between both solid constituents with respect to their weight ratio (here 1:0.8). As case ii we assume that the entire solvent is available for each solid compound. Both cases assume ideal polymer–fullerene interaction. That means P3HT and PCBM interacts with its own type of molecules in the same manner as with the other type of molecule. The verification or falsification of this hypothesis is discussed below and provides information on the real polymer–fullerene interaction forces in the ternary solution and the transferability of the binary data to the ternary system. The expected ranges of transitions in Figure 3a are compared with the observed evolution of P3HT crystallinity (Figure 3b) for the investigated ternary system. The measure of P3HT crystallinity is obtained from the integrated intensity of the P3HT (100) Bragg peak. For P3HT, we initially expect a delay in crystallization until the solubility limit is reached. Regarding the marginally decreasing solvent fraction in this period, P3HT nucleation at the solubility limit is expected for the solid mass fraction $x_s = 5.1-9.1$ wt % (according to the binary phase diagrams and cases i and ii) which is confirmed by the appearance of the P3HT (100) Bragg peak after 156 s ($x_s = 4.6$ wt %) of film drying. The integrated Bragg–Peak intensity of P3HT is low at this early stage of nucleation. Subsequently the intensity increases and near the range of complete gelation, the second and third order Bragg peaks appear, indicating further crystallization. When the film is dry, the intensity of the P3HT (100) Bragg peak also remains almost constant. A slight intensity increase afterward may be attributed to molecular ordering under the influence of the remanent solvent vapor in the atmosphere.

It was observed that PCBM crystallizes at a later stage of drying. Though the DCB and PCBM diffraction peaks nearly overlap, profile plots in Figure 3c show the emergence of the diffraction peak of PCBM after the disappearance of the DCB diffraction peaks (due to the evaporation of the solvent DCB during drying). The overlap of the PEDOT:PSS and the PCBM diffraction peaks makes it difficult to decipher the appearance of the PCBM peak following the disappearance of DCB diffraction peaks. Hence, the profile plots in Figure 3c were taken without PEDOT:PSS on a silicon substrate (with native silicon dioxide) as the only exception within this work. The P3HT (100) Bragg peak at $q = 0.4$ A^{-1} appears at 702 s drying time ($x_s = 14$ wt %), while the PCBM diffraction peak at $q = 1.36$ A^{-1} starts to form at 864 s ($x_s = 46$ wt %). Even for the highest published

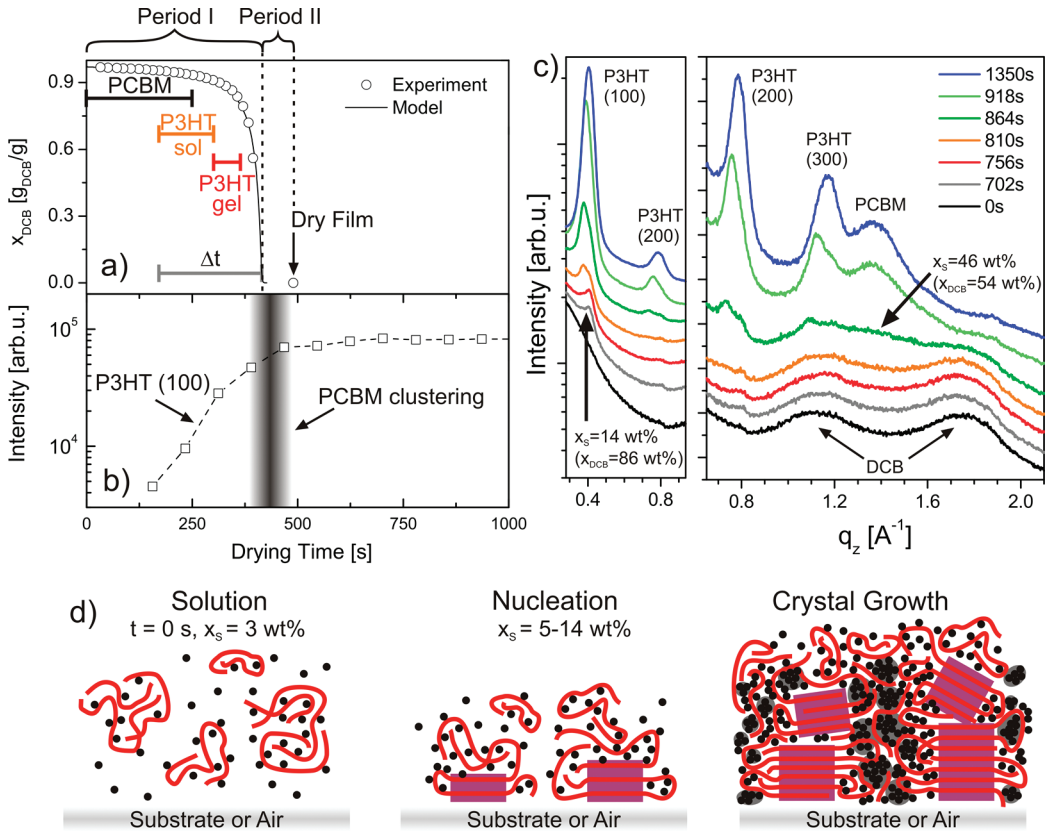

Figure 3. (a) Evolution of film composition (solvent mass fraction x_{DCB}) during film drying of doctor-bladed P3HT:PCBM films on PEDOT:PSS/glass as obtained from laser reflectometry (data, symbols; fit from model, line). The labeled bars indicate ranges of phase transitions as expected from the superposition of the binary phase diagrams. Two different drying phases are marked as period I (constant rate period) and period II (falling rate period). Period II is determined experimentally from the time period between last interference peak and a constant reflectometer signal. The constant rate period time after crossing P3HT solubility is denoted as Δt. (b) To obtain the measure of overall P3HT crystallinity in the blend film, the integrated area of the P3HT (100) Bragg peak is plotted *versus* drying time. (c) Selected profile plots at increasing drying times showing the emergence of the diffraction peaks of PCBM, P3HT (h00) Bragg peaks and disappearance of the diffraction peaks of the evaporating solvent DCB on a silicon dioxide/silicon substrate (log scale left, linear right). These were the only measurements not carried out on PEDOT:PSS. (d) Scheme shows the stages of molecular arrangement during solvent evaporation with nucleation at the substrate or air interface. Lines represent P3HT chains, purple squares are crystalline P3HT domains, and dots are PCBM molecules.

PCBM solubility of about 100 mg/mL[33] (x_s = 7.7 wt % at room temperature) PCBM would be expected to crystallize at an earlier stage. This is giving evidence that polymer crystallization occurs first, followed by PCBM clustering at a later stage of drying. These observations of suppressed PCBM crystallization suggest that strong interactions between fullerene and polymer molecules exist. Hence the polymer–fullerene interactions prevail over the fullerene–fullerene interactions. This is supported by the observation of large micrometer-sized PCBM crystallites if the polymer is absent.[43]

PCBM cannot intercalate P3HT crystallites due to limited space in between the alkyl side chains.[45] This was confirmed by Collins *et al.* who showed that in thermodynamic equilibrium P3HT crystallites only comprise 3–4% PCBM.[46] Our observations suggest that PCBM molecules are squeezed out of the area where the polymer crystallizes during drying which is followed by subsequent fullerene aggregation. Hence, the phase separation mechanism of P3HT:PCBM blends during film drying seems to be rather driven by crystallization than by spinodal decomposition.

As mentioned before, the spot-like P3HT (100) Bragg peak shown in Figure 2d at 156 s indicates that the initially formed P3HT nuclei are very well aligned in an edge-on configuration as depicted in Figure 2b.[38,47] This implies that the well-aligned nucleation is induced by a planar interface, plausibly at the film–substrate or film–air interface. Starting at the well-oriented layer, further polymer crystallizes, whereby the subsequently formed P3HT crystallites exhibit an increasing orientation distribution, which can be seen in an increasing wing-like (100) Bragg peak shape with proceeding solvent evaporation in Figure 2d.

The structure evolution of the blend is schematically shown in Figure 3d, where PCBM is symbolized as dots, P3HT as lines and purple rectangles symbolizing crystalline P3HT domains. Collins *et al.* observed a solubility of about 16% in amorphous P3HT regions,

in contrast to a low PCBM solubility of only 3−4% in crystalline P3HT. These findings are in agreement with a picture of three coexisting phases: (a) mainly pure crystalline P3HT domains comprising very few PCBM inclusions, (b) amorphous P3HT regions containing higher amounts of PCBM molecules which could not be removed from the polymer chains by crystallization processes due to strong P3HT−PCBM interactions, and (c) PCBM clusters partly intermixed in the amorphous P3HT regions which enrich with PCBM that is being displaced out of the regions where P3HT crystallizes.

Drying Process−Morphology Relationship. It is of great interest to investigate how changes of solubility and crystallization brought about by temperature and nitrogen flow affect the final film morphology and solar cell performance. To investigate the effect of these two parameters, P3HT:PCBM films were fabricated under different drying conditions: 15, 25, and 40 °C drying temperature and 0.15 and 0.5 m/s nitrogen flow velocity.

We observed that the final dried films showed high peak−valley roughness of about 200 nm at low drying temperatures. Consequently, for this study, films were prepared at thicknesses of 350 nm (±28 nm) in order to prevent local shortcuts caused by very thin active layers. In this thickness range, the absorption and solar cell efficiency exhibit a broad plateau,[48] diminishing the influence of thickness fluctuations. The drying kinetics of the P3HT:PCBM films were calculated according to ref 37 and are shown in Figure 4, where the solvent mass fraction is plotted *versus* drying time. Both temperature and gas flow rate affect the overall drying time for film formation, that is, faster gas velocity or higher temperature leads to a faster drying.

The morphology of the dried films was investigated by AFM (surface) and STEM (transmission, see Supporting Information). AFM measurements give evidence of the existence of two different morphology length scales by comparing the topography (Figure 5a) with the phase image (Figure 5b). While the dominating lateral structures of film topography measure up to several hundred nanometers, we observe a smaller substructure in the phase image which resembles the nanofibril structure of P3HT reported by Zhang *et al.*[19] On the one hand, obtained AFM phase images do not show any systematic influence of drying conditions on the fibril structure of P3HT in the blend with PCBM. On the other hand, lateral and vertical dimensions of topological features increase with drying time after crossing P3HT solubility (denoted as Δt in Figure 3a). This is manifested in the roughness of the films dried under different temperature and drying rate conditions, shown in Figure 5c (filled symbols). In the absence of PCBM, neat P3HT-films (open symbols) show similar values of roughness, demonstrating that the film topography is mainly governed by the dynamics of P3HT assembly. To explain the origin of film morphology, the identification of the driving force for structure

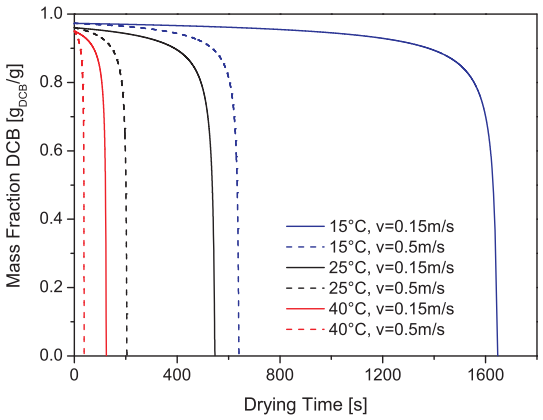

Figure 4. Calculated drying kinetics of P3HT:PCBM films at different drying temperatures and drying gas velocities.

formation and its relation to the drying conditions and phase behavior is crucial. Kim *et al.* proposed the film morphology of conjugated polymer blends to originate from spinodal demixing.[44] This process of spinodal demixing was further investigated by Heriot *et al.* who observed a bilayer formation in polymer−polymer blends with subsequent stratification during film drying leading to a phase separated morphology.[49] Likewise, an investigation of P3HT:PCBM blends with laser reflectometry did not show any evidence of a bi- or multilayer formation.[15] Hence, we assume that the observed large-scale morphology features predominantly form as result of growing polymer aggregates; the aggregate size seems to depend on drying time after crossing P3HT solubility.

Figure 5d schematically illustrates the formation of a smooth film without P3HT aggregation in fast drying conditions. Figure 5e schematically shows the formation of a rough film in slow drying conditions due to the growth of P3HT aggregates in the course of drying. This systematic roughness effect might be used for the enlargement of the active layer/metal electrode contact area and for ameliorated light absorption[50] without any additional processing steps.

It is worthwhile to mention that PCBM solubility increases stronger with temperature than P3HT does. For instance from 10 to 40 °C solubility grows about a factor of 2.4 and 2.7 for P3HT and PCBM, respectively (Figure 1). Increased solubility signifies increased solvent−solid interaction which leads in the case of P3HT:PCBM to a weakened polymer−fullerene interaction at higher temperatures. This possibly elucidates the previously observed effect of larger PCBM aggregates in 40 °C processed films.[40]

The coating quality (thickness homogeneity at centimeter scale) by doctor blading was best at 15 °C, because of the higher viscosity and early gelation of the solution, which suppressed dewetting effects due to inertial forces (increased viscosity). Koppola *et al.* observed an improvement of film homogeneity by increasing the solid fraction to 8−12 wt % at room

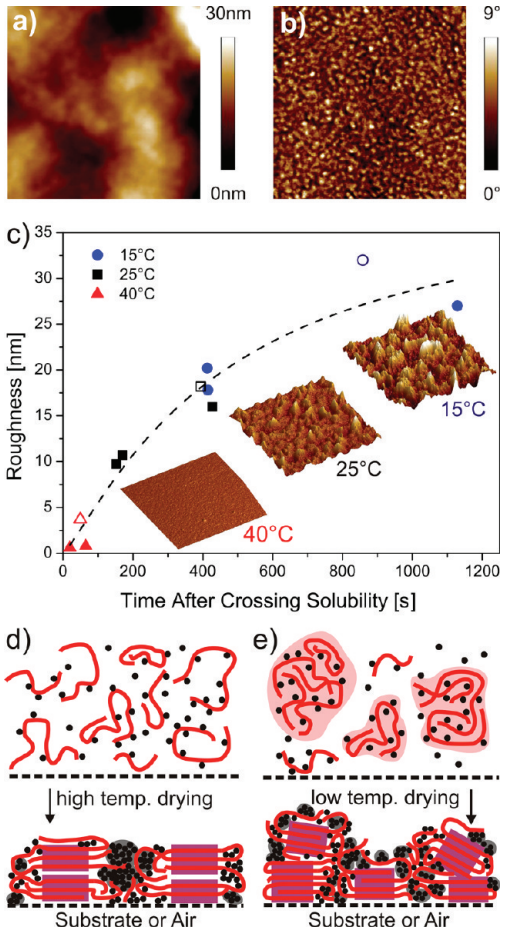

Figure 5. Influence of drying conditions on the topography for the investigated P3HT:PCBM films on PEDOT:PSS/ITO/glass substrates. The different dimensions of (a) the topography and (b) the fibril structure in the AFM phase image for 25 °C, v = 0.5 m/s drying conditions. The image dimensions are 1 μm × 1 μm. (c) Influence of drying time after crossing P3HT solubility (Δt) on final film roughness for pure P3HT (open symbols) and P3HT:PCBM (filled symbols) films dried at different conditions and substrate positions. The AFM insets represent 10 μm × 10 μm P3HT:PCBM surfaces with a height scale of 150 nm. The film thicknesses are 350 ± 28 nm. (d) Schematic of molecular ordering for fast drying in comparison to (e) slow drying with larger-scale polymer aggregation leading to high film roughness. The P3HT–PCBM phase segregation results in a smaller substructure within the film topography.

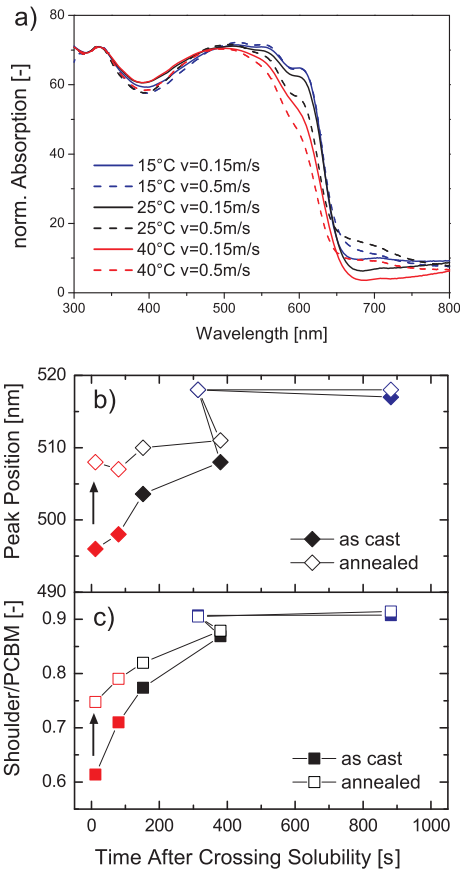

Figure 6. (a) Absorption spectra of P3HT:PCBM films dried at 15 °C (blue), 25 °C (black), 40 °C (red) drying temperature at a nitrogen flow of 0.15 m/s (solid lines) and 0.5 m/s (dashed lines). The spectra are normalized to the PCBM peak at 333 nm. (b) Position of the P3HT main absorption peak and (c) absorption ratio of the vibronic shoulder at 605 nm related to the constant PCBM absorption at 333 nm for the as-cast (filled symbols) and annealed (150 °C, 5 min, open symbols) films plotted against the drying time after crossing P3HT solubility.

temperature rather than by decreasing the temperature.[51] This is most probably due to the same effect of increased viscosity or even a gel formation by entering the two phase region for P3HT (Figure 1b).

Optoelectronic Properties. To correlate the discussed structural study with optoelectronic device properties, solar cells were built under the same coating and drying conditions resulting in the same layer thicknesses as for the films investigated above. Decreasing drying temperature and increasing drying time (slowly dried films) shifts the P3HT main absorption peak to longer wavelength and enhances the vibronic shoulders in the absorption spectra (Figure 6a). The position of the P3HT main absorption peak is plotted against the drying time after crossing P3HT solubility in Figure 6b. A shift to longer wavelength originates from a higher effective conjugation length of the polymer backbone and hence more linearly stretched polymers as well as from enhanced interchain interactions,[38,52] which we observe in slowly dried films at low temperatures. After annealing the films at 150 °C for 5 min, the position of the P3HT main absorption peak is independent from the drying gas velocity at each temperature, leading to the assumption that the correlation length is merely related to drying temperature. As a measure for the vibronic shoulders, which correlate with the amount of $\pi-\pi$ interchain stacked P3HT molecules,[40,53] we chose the ratio of the $\pi-\pi$ absorption at 605 and 333 nm (PCBM). The amount of interchain P3HT $\pi-\pi$ ordering increases with overall drying time after crossing P3HT solubility, but approaches a saturation value for 15 °C drying temperature (blue symbols in Figure 6c). A similar behavior is observed for the peak position. This seems to indicate that P3HT crystallization reaches

saturation after a certain time (in this case 300 s). Additional thermal annealing enhances the shoulder for fast dried films, but this effect gets negligible for longer drying times.

The corresponding current density–voltage characteristics of the respective solar cells are shown in Figure 7a. All layers except the cathode were prepared in ambient conditions which causes drawbacks in open circuit voltage and power conversion efficiency (PCE). The highest PCE of 2.1% for the untreated, doctor-bladed solar cells was achieved at 15 °C and 0.15 m/s drying gas velocity. The solar cell efficiencies increase with lower drying temperature and thus with longer crystallization time after crossing P3HT solubility (Table 1). The gain in efficiency is mainly due to an increased short circuit current density (Figure 7b). It is remarkable that this trend is still existent after annealing for 5 min at 150 °C. As depicted in Figure 7 panels b and c, the short circuit current density and the PCE of both the 15 °C (fast and slow gas flow) and the slowly dried 25 °C solar cell are very similar. This depicts the same saturation trend as observed before for the optical properties.

These results suggest that sufficiently slow drying at low temperatures allows the polymer molecules to assemble and reach a favorable nanomorphology. In preceding work we have shown that lower drying temperature also causes a finer P3HT-PCBM phase separation and a larger angular orientation distribution of P3HT crystallites.[40] Additionally, the high surface roughness might increase the PCE with increased light trapping and contact area to the cathode layer. In contrast, in fast drying conditions, the higher solvent evaporation rate reduces the time for structure formation, leading to a lower degree of interchain P3HT $\pi-\pi$ ordering, a lower surface roughness and consequently a lower PCE. This also leads to an increased series resistance for fast dried P3HT:PCBM layers; this can be derived from the slope of the current density–voltage curve in the forward operation regime in Figure 7a.

The improved PCE (Figure 7c) due to thermal annealing comprises an almost constant increase of short circuit current at all drying conditions. For the 15 °C processed devices, the performance improvement is not due to changes in the optical properties since they remain constant upon annealing (Figure 6b,c). A possible explanation could be an improved active layer/cathode contact after the thermal treatment and the removal of residual solvent and/or humidity. Despite thermal annealing, the trend of higher PCE at lower drying temperatures and rates remains, identifying the

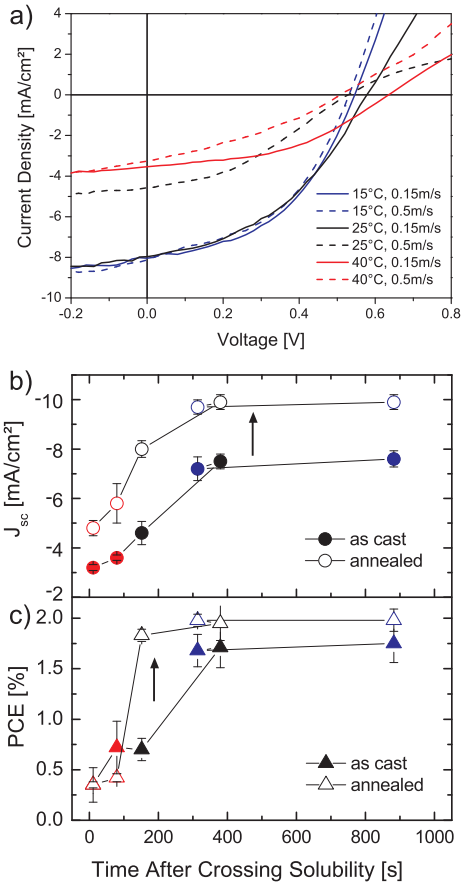

Figure 7. (a) Current density–voltage characteristics of the best untreated P3HT:PCBM devices dried at 15 °C (blue), 25 °C (black), or 40 °C (red) drying temperature at a nitrogen flow of 0.15 m/s (solid lines) and 0.5 m/s (dashed lines). (b) Short circuit current density and (c) power conversion efficiency of the respective untreated (filled symbols) and annealed for 5 min at 150 °C (open symbols) solar cells plotted against the drying time after crossing P3HT solubility.

TABLE 1. Device Performance of the Untreated P3HT:PCBM Films Fabricated by Doctor Blading in Ambient Conditions at Different Drying Scenarios[a]

as cast drying conditions	thickness [nm]	J_{sc} [mA/cm^2]	V_{oc} [V]	FF [%]	η [%]	η_{max} [%]
15 °C, v = 0.15 m/s	308	−7.6 ± 0.3	0.52 ± 0.02	44.2 ± 2.3	1.8 ± 0.2	2.1
15 °C, v = 0.5 m/s	262	−7.2 ± 0.5	0.52 ± 0.02	45.2 ± 4.1	1.7 ± 0.2	2.0
25 °C, v = 0.15 m/s	362	−7.5 ± 0.3	0.55 ± 0.04	41.3 ± 1.9	1.7 ± 0.2	2.0
25 °C, v = 0.5 m/s	346	−4.6 ± 0.5	0.44 ± 0.07	34.8 ± 3.8	0.7 ± 0.1	0.9
40 °C, v = 0.15 m/s	439	−3.6 ± 0.1	0.53 ± 0.12	37.1 ± 7.0	0.7 ± 0.3	1.0
40 °C, v = 0.5 m/s	151	−3.2 ± 0.1	0.35 ± 0.14	30.1 ± 3.7	0.4 ± 0.2	0.6

[a] Poor wetting properties at 40 °C coating and drying conditions led to inhomogeneous thicknesses. Device characterization was performed in an N_2 atmosphere at room temperature.

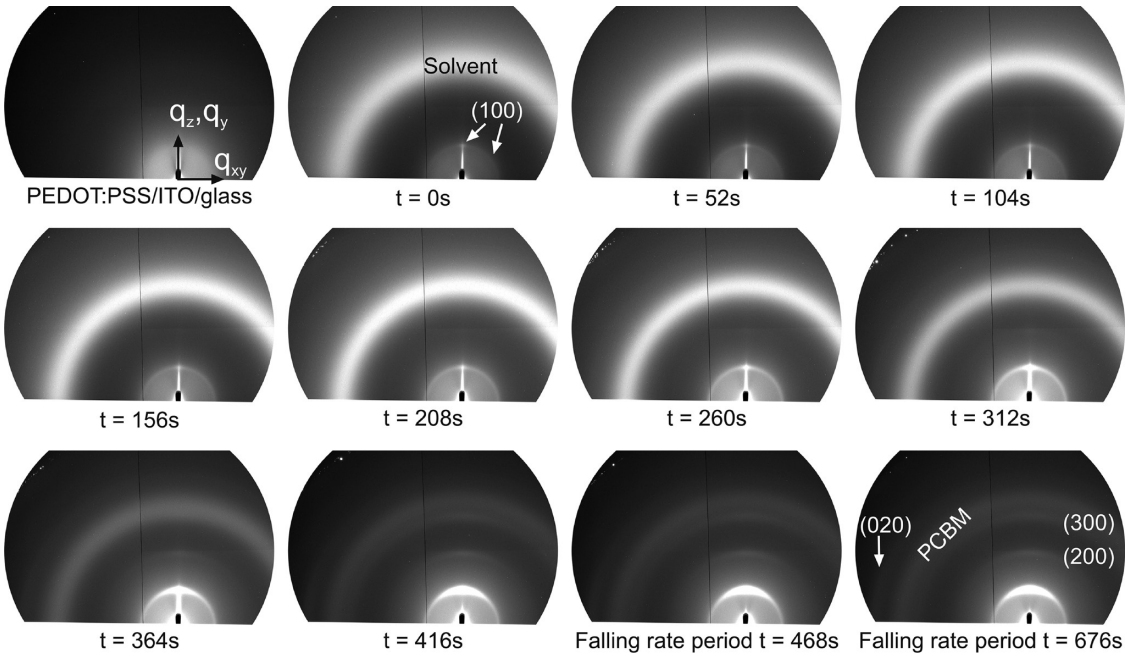

Figure 8. Real time 2D GIXD diffraction patterns collected during drying of P3HT:PCBM (1:0.8) (d = 213 nm, R_q = 51 nm) cast from a 1:1 mixture of chlorobenzene (CB) and cyclohexanone (CHN) at a substrate temperature of 15 °C. While the first image is of the PEDOT:PSS/ITO/glass substrate, the subsequent images show the evolution of film drying and crystallization. Below each image, the drying time is mentioned. The onset of the falling rate drying regime is at about 450 s.

drying process as an additional key for the manipulation of the film morphology and hence the solar-cell properties. The low sensitivity of PCE on the drying gas flow at 15 °C is attractive for large area roll-to-roll solar-cell fabrication, where an inhomogeneous gas flow in the drying unit could affect laterally inhomogeneous film drying rates.

Crystallization of Polymer–Fullerene Dispersions from a Solvent Mixture. As mentioned above, we observed the onset of P3HT crystallization at a film composition in the range of its solubility limit. This observation provides important information about the blend crystallization. The initial drying period prior crossing P3HT solubility does not contribute to the blend crystallization. Hence, slow drying seems to be unnecessary in this region of the phase diagram. For a reduction of the initial drying phase before crossing P3HT solubility, one can reduce drying temperature in order to shift the solubility limit to an earlier stage of the drying process as we have previously shown. Unfortunately this has the consequence of reduced solvent vapor pressure which results in low fabrication speeds due to slow drying.

Another strategy is altering the thermodynamics of phase separation by the addition of an "unfriendly" solvent for both components which reduces the solubility of P3HT and PCBM and induces partially ordered aggregates in solution. It is important that the "unfriendly" solvent exhibits a lower vapor pressure as the "friendly" solvent in order to prevent redissolution of the previously formed aggregates. Following this idea, several groups prepared such P3HT:PCBM dispersions by adding for instance nitrobenzene (NtB)[54] or cyclohexanone (CHN)[55] to chlorobenzene (CB), yielding P3HT:PCBM films with improved solar cell performance.

By adding the "unfriendly" solvent cyclohexanone to the chlorobenzene solution of P3HT:PCBM the solubility can be crossed already in the solution preparation step. We have monitored in real-time by GIXD the structural evolution of P3HT:PCBM during film formation from a solvent mixture of CHN:CB (1:1). The GIXD patterns obtained directly after coating (t = 0) already exhibits the P3HT (100) Bragg reflection. It is important to note that the wing-like spread of the (100) Bragg peak covers the entire angular distribution of ±90°. This confirms the crystallization of randomly oriented, solid-like P3HT aggregates in the dispersion, presumably forming fibrils accordingly to previous works.[55] This is in contrast to the structural evolution from regular CB and DCB solutions where P3HT crystallization is interface-induced which results in a predominant (100) orientation at the early stages of film formation. The comparison of the GIXD patterns in an early stage of drying is shown in Figure 9 panels a and b for DCB and CB-CHN, respectively, and is schematically illustrated in panels c and d. As the solvent evaporates (Figure 8), ongoing P3HT crystallization is observed with a large distribution of orientations deviating from the spot-like (100) Bragg peak in out of plane direction (Figure 8). The broad orientation distribution is also reflected in the azimuthal spread of the P3HT (020) peak, associated with the polymer $\pi-\pi$ stacking. This can result

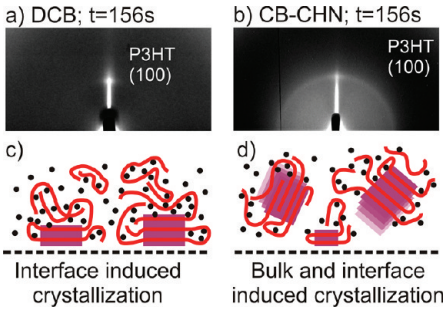

Figure 9. GIXD snapshots of P3HT:PCBM blend crystallization in films cast from (a) DCB and (b) CB-CHN. For DCB the spotlike peak indicates interface-induced crystallization while a broad diffraction ring for the CB-CHN dispersion indicates additional bulk crystallization like schematically depicted in panels c and d, respectively. The lamellae $\pi-\pi$ stacking direction is normal to the image plane.

in higher hole mobilities perpendicular to the substrate in contrast to the edge-on oriented configuration formed from regular DCB solution where high hole mobility is only expected along the substrate.

The growth of P3HT domains from preformed aggregates in solution (serving as growth nuclei) and from nucleation at the interface give rise to blends with relatively large P3HT crystallinity and orientational disorder. Berson *et al.* demonstrated the importance of having an amorphous component mixed among the fibers to obtain high efficiency solar cells.[56] Thus it is reasonable to hypothesize that regions of disordered P3HT among the crystalline P3HT fibers positively contribute to electronic connectivity among crystalline domains.

Hence, the formation of randomly oriented P3HT crystallites dispersed in disordered P3HT and PCBM—in contrast to the interface induced edge-on growth from pure DCB—is assumed to be responsible for the increased vertical hole mobility and improved power conversion efficiency of about 4% reported for P3HT:PCBM dispersions cast from CB-NtB[54] and CB-CHN.[55]

CONCLUSION

The pathway through the phase diagrams of P3HT and PCBM solutions was compared with the structural changes during crystallization of the ternary P3HT:PCBM blend observed in real time by GIXD. It could be shown that PCBM crystallizes at the final stage of drying although its solubility is reached in a very early stage. This demonstrates strong polymer−fullerene interactions that impede the crystal growth of PCBM. The film roughness is shown to depend on the drying time after crossing P3HT solubility. For low drying temperatures and slow drying gas velocities, higher PCEs are observed, which is also related to a stronger P3HT interchain $\pi-\pi$-ordering.

The addition of CHN as "unfriendly solvent" to CB allows crossing the solubility limit of P3HT before film drying has started. This induces partial P3HT aggregation in solution. *In-situ* observation of the film formation by GXID reveals a broader orientation distribution of P3HT crystallites for such dispersions in comparison to the interface-induced crystallization from CB or DCB. We suggest that this enhances the vertical charge transport along the polymer backbones and along the $\pi-\pi$ stacking direction which consequently leads to more efficient solar cells.

This work gains understanding of thermodynamic and solvent drying kinetics effects for morphology control and their impact on the device performance.

EXPERIMENTAL METHODS

Phase Diagrams. For the determination of the binary P3HT (Rieke Metals 4002E, $M_w \approx 48900$ g/mol, polydispersity = 1.7) DCB (anhydrous 99%, Sigma Aldrich) phase diagram, slightly oversaturated solutions were prepared such that a solid-rich gel phase was formed in addition to the solid-poor solution phase. This was accomplished under permanent mixing on a lab shaker for 18 h in a temperature controlled environment where the temperature was set constant to the respectively desired value from 0 to 60 °C. Koppe *et al.* observed completed gelation after a maximum of 16 h for several molecular weights of P3HT.[18] In a subsequent temperature controlled centrifugation step (Sigma 2-16KCH), sol and gel phase were separated at the respective equilibrium temperatures (0−60 °C). Before extracting sol and gel samples with a syringe out of each phase, the solution rested a further 2 h at the adjusted temperature in order to diminish the influence of shear forces during the centrifugation step. After diluting the extracted samples, the refractive index of the solution was determined with an Abbe refractrometer (Dr. Kernchen) to obtain the mass fraction of the solution using a previous calibration. Likewise the analysis of PCBM (Solenne, purity >99%) solubility was done. In this case only the solution phase was analyzed. All process steps and measurements were conducted four times from independently prepared samples.

GIXD Measurements. The real-time GIXD study was done at beamline ID10B with energy 12.3 keV in the European Synchrotron Radiation Facility (ESRF), Grenoble, France, during the evaporation of the solvent in a temperature-controlled environment utilizing poly(3,4-ethylenedioxythiophene):poly(styrenesulfonate) (PEDOT:PSS, H.C. Starck, Clevios VP AI 4083)-coated glass slides or native silicon wavers as substrates. The X-ray diffraction patterns of the drying blend film were taken with an area detector (MarCCD) with 3 s of integration time in intervals of 50 s.[40] The sample preparation was the same as that for solar-cell fabrication. The P3HT:PCBM dispersion in CB-CHN (1:1 by volume) was prepared according to Kim and co-workers.[55] First a 2.5 wt % solution of P3HT:PCBM in CB was prepared and subsequently diluted with CHN. After stirring about 2 h the dispersion was cast and dried at 15 °C on PEDOT:PSS/ITO/glass substrates.

Preparation of Solar Cells. For the sample preparation, we used 48 mm × 60 mm ITO/glass substrates (12 Ω/□, Visiontek) except for the *in situ* GIXD measurements where we used float glass slides (35 mm × 60 mm). The substrates were cleaned by sonication in acetone and isopropyl alcohol, followed by an oxygen plasma treatment. Subsequently the PEDOT:PSS dispersion was coated by doctor blading in ambient conditions. 40 μL PEDOT:PSS dispersion (diluted 1:1 by volume with water) were cast with a blade slit width of 70 μm and a blade speed

of 5 mm/s resulting in 20−40 nm dry film thickness. This layer was subsequently heated at 120 °C for 20 min in a glovebox under nitrogen atmosphere. P3HT and PCBM with weight ratios of 1:0.8 were dissolved in 2.7 to 5 wt % solid fraction in DCB (depending on the coating temperature) and cast using the same parameters as for the PEDOT:PSS layer in the setup shown in Figure 2a. The coating parameters and setup were the same for *in situ* GIXD measurements and solar cell preparation. After cutting the substrates into 16 mm × 16 mm pieces, a calcium (50 nm)/aluminum (200 nm) cathode was deposited through a shadow mask.

AFM Measurements. AFM measurements were done in tapping mode with a Veeco Dimension Icon. The root-mean-square roughness analysis was done on 10 μm × 10 μm images of the final films.

Absorption Spectra. The absorption was measured in transmission with a spectrophotometer (Perkin-Elmer, Lambda 1050) using a blank PEDOT:PSS/ITO/glass substrate as reference. The absorption spectra were normalized to the PCBM absorption peak at 333 nm. The samples were taken from the same 48 mm × 60 mm substrates that were used for the solar cell devices.

Solar Cells Characterization. The current density−voltage characteristics were measured under a spectrally monitored ORIEL solar simulator (1 sun according to ASTM-G173−03el) under nitrogen atmosphere. The active area was 0.24 cm^2.

Acknowledgment. The present work was supported by the German Research Foundation (DFG) within the Priority Program 1355 "Elementary processes of organic photovoltaics". We acknowledge the European Synchrotron Radiation Facility (ESRF) for provision of synchrotron radiation facilities. The authors thank H. Hölscher and the Karlsruhe Nano and Micro Facility (KNMF) for providing access to the AFM, N. Mechau for affording thickness measurements with a Dektak 6M, and S. Walheim, M. Kowalski, and F. Pasker for their support.

Supporting Information Available: Further details on the phase diagrams as well as additional AFM and STEM images of the investigated P3HT:PCBM films. This material is available free of charge *via* the Internet at http://pubs.acs.org.

REFERENCES AND NOTES

1. Krebs, F. C. Fabrication and Processing of Polymer Solar Cells: A Review of Printing and Coating Techniques. *Sol. Energy Mater. Sol. Cells* **2009**, *93*, 394–412.
2. Krebs, F. C.; Tromholt, T.; Jørgensen, M. Upscaling of Polymer Solar Cell Fabrication Using Full Roll-to-Roll Processing. *Nanoscale* **2010**, *2*, 873–886.
3. Moulé, A. J.; Meerholz, K. Controlling Morphology in Polymer−Fullerene Mixtures. *Adv. Mater.* **2008**, *20*, 240–245.
4. van Bavel, S. S.; Sourty, E.; de With, G.; Loos, J. Three-Dimensional Nanoscale Organization of Bulk Heterojunction Polymer Solar Cells. *Nano Lett.* **2009**, *9*, 507–513.
5. Slota, J. E.; Hea, X.; Huck, W. T. S. Controlling Nanoscale Morphology in Polymer Photovoltaic Devices. *Nano Today* **2010**, *5*, 231–242.
6. Haugeneder, A.; Neges, M.; Kallinger, C.; Spirkl, W.; Lemmer, U.; Feldmann, J.; Scherf, U.; Harth, E.; Gügel, A.; Müllen, K. Exciton Diffusion and Dissociation in Conjugated Polymer/Fullerene Blends and Heterostructures. *Phys. Rev. B* **1999**, *59*, 15346–15351.
7. Lunt, R. R.; Giebink, N. C.; Belak, A. A.; Benziger, J. B.; Forrest, S. R. Exciton Diffusion Lengths of Organic Semiconductor Thin Films Measured by Spectrally Resolved Photoluminescence Quenching. *J. Appl. Phys.* **2009**, *105*, 053711.
8. Yang, L. G.; Chen, H. Z.; Wang, M. Optimal Film Thickness for Exciton Diffusion Length Measurement by Photocurrent Response in Organic Heterostructures. *Thin Solid Films* **2008**, *516*, 7701–7707.
9. Shaheen, S. E.; Brabec, C. J.; Sariciftci, N. S.; Padinger, F.; Fromherz, T.; Hummelen, J. C. 2.5% Efficient Organic Plastic Solar Cells. *Appl. Phys. Lett.* **2001**, *78*, 841–843.
10. Merlo, J. A.; Frisbie, C. D. Field Effect Conductance of Conducting Polymer Nanofibers. *J. Polym. Sci. Part. B: Polym. Phys.* **2003**, *41*, 2674–2680.
11. Li, G.; Shrotriya, V.; Huang, J.; Yao, Y.; Moriarty, T.; Emery, K.; Yang, Y. High-Efficiency Solution Processable Polymer Photovoltaic Cells by Self-Organization of Polymer Blends. *Nat. Mater.* **2005**, *4*, 864–868.
12. Mihailetchi, V. D.; Xie, H.; Boer, B.; Popescu, L. M.; Hummelen, J. C.; Blom, P. W. M. Origin of the Enhanced Performance in Poly(3-hexylthiophene):[6,6]-Phenyl C61-Butyric Acid Methyl Ester Solar Cells upon Slow Drying of the Active Layer. *Appl. Phys. Lett.* **2006**, *89*, 012107.
13. Schmidt-Hansberg, B.; Do, H.; Colsmann, A.; Lemmer, U.; Schabel, W. Drying of Thin Film Polymer Solar Cells. *Eur. Phys. J. Spec. Top.* **2009**, *166*, 49–53.
14. Lin, C.; Lin, E. Y.; Tsai, F. Y. Enhanced Thermal Stability and Efficiency of Polymer Bulk-Heterojunction Solar Cells by Low-Temperature Drying of the Active Layer. *Adv. Funct. Mater.* **2010**, *20*, 834–839.
15. Schmidt-Hansberg, B.; Klein, M. F. G.; Peters, K.; Buss, F.; Pfeifer, J.; Walheim, S.; Colsmann, A.; Lemmer, U.; Scharfer, P.; Schabel, W. *In Situ* Monitoring the Drying Kinetics of Knife Coated Polymer−Fullerene Films for Organic Solar Cells. *J. Appl. Phys.* **2009**, *106*, 124501.
16. Troshin, P. A.; Hoppe, H.; Renz, J.; Egginger, M.; Mayorova, J. Y.; Goryachev, A. E.; Peregudov, A. S.; Lyubovskaya, R. N.; Gobsch, G.; Sariciftci, N. S.; *et al.* Material Solubility-Photovoltaic Performance Relationship in the Design of Novel Fullerene Derivatives for Bulk Heterojunction Solar Cells. *Adv. Funct. Mater.* **2009**, *19*, 779–788.
17. Malik, S.; Jana, T.; Nandi, A. K. Thermoreversible Gelation of Regioregular Poly(3-hexylthiophene) in Xylene. *Macromolecules* **2001**, *34*, 275–282.
18. Koppe, M.; Brabec, C. J.; Heiml, S.; Schausberger, A.; Duffy, W.; Heeney, M.; McCulloch, I. Influence of Molecular Weight Distribution on the Gelation of P3HT and Its Impact on the Photovoltaic Performance. *Macromolecules* **2009**, *42*, 4661–4666.
19. Zhang, R.; Li, B.; Iovu, M. C.; Jeffries-EL, M.; Sauvé, G.; Cooper, J.; Jia, S.; Tristram-Nagle, S.; Smilgies, D. M.; Lambeth, D. N.; McCullough, R. D.; *et al.* Nanostructure Dependence of Field-Effect Mobility in Regioregular Poly(3-hexylthiophene) Thin Film Field Effect Transistors. *J. Am. Chem. Soc.* **2006**, *128*, 3480–3481.
20. Reyes-Reyes, M.; Kim, K.; Carroll, D. L. High-Efficiency Photovoltaic Devices Based on Annealed Poly(3-hexylthiophene) and 1-(3-methoxycarbonyl)-propyl-1-phenyl-(6,6)C61 Blends. *Appl. Phys. Lett.* **2005**, *87*, 083506.
21. Yang, X.; Loos, J.; Veenstra, S. C.; Verhees, W. J. H.; Wienk, M. M.; Kroon, J. M.; Michels, M. A. J.; Janssen, R. A. J. Nanoscale Morphology of High-Performance Polymer Solar Cells. *Nano Lett.* **2005**, *5*, 579–583.
22. Ma, W.; Yang, C.; Gong, X.; Lee, K.; Heeger, A. J. Thermally Stable, Efficient Polymer Solar Cells with Nanoscale Control of the Interpenetrating Network Morphology. *Adv. Funct. Mater.* **2005**, *15*, 1617–1622.
23. Mihailetchi, V. D.; Xie, H.; Boer, B.; Koster, L. J. A.; Blom, P. W. M. Charge Transport and Photocurrent Generation in Poly(3-hexylthiophene):Methanofullerene Bulk-Heterojunction Solar Cells. *Adv. Funct. Mater.* **2006**, *16*, 699–708.
24. Verploegen, E.; Mondal, R.; Bettinger, C. J.; Sok, S.; Toney, M. F.; Bao, Z. Effects of Thermal Annealing Upon the Morphology of Polymer−Fullerene Blends. *Adv. Funct. Mater.* **2010**, *20*, 3519–3529.
25. Zhao, Y.; Xie, Z.; Qu, Y.; Geng, Y.; Wang, L. Solvent-Vapor Treatment Induced Performance Enhancement of Poly(3-Hexylthiophene):Methanofullerene Bulk-Heterojunction Photovoltaic Cells. *Appl. Phys. Lett.* **2007**, *90*, 043504.
26. Sharma, G. D.; Suresh, P.; Sharma, S. S.; Vijay, Y. K.; Mikroyannidis, J. A. Effect of Solvent and Subsequent Thermal Annealing on the Performance of Phenylenevinylene Copolymer:PCBM Solar Cells. *Appl. Mater. Interfaces* **2010**, *2*, 504–510.
27. van Bavel, S. S.; Sourty, E.; de With, G.; Loos, J. Three-Dimensional Nanoscale Organization of Bulk Heterojunction Polymer Solar Cells. *Nano Lett.* **2009**, *9*, 507–513.

28. Pfaff, M.; Müller, E.; Klein, M. F. G.; Colsmann, A.; Lemmer, U.; Krzyzanek, V.; Reichelt, R.; Gerthsen, D. Low-Energy Electron Scattering in Carbon-Based Materials Analyzed by Scanning Transmission Electron Microscopy and Its Application to Sample Thickness Determination. *J. Microsc.* **2011**, *243*, 31–39.
29. Müller, C.; Ferenczi, T. A. M.; Campoy-Quiles, M.; Frost, J. M.; Bradley, D. D. C.; Smith, P.; Stingelin-Stutzmann, N.; Nelson, J. Binary Organic Photovoltaic Blends: A Simple Rationale for Optimum Compositions. *Adv. Mater.* **2008**, *20*, 3510–3515.
30. Zhao, J.; Swinnen, A.; Van Assche, G.; Manca, J.; Vanderzande, D.; Van Mele, B. Phase Diagram of P3HT/PCBM Blends and Its Implication for the Stability of Morphology. *J. Phys. Chem. B* **2009**, *113*, 1587–1591.
31. Hopkinson, P. E.; Staniec, P. A.; Pearson, A. J.; Dunbar, A. D. F.; Wang, T.; Ryan, A. J.; Jones, R. A. L.; Lidzey, D. G.; Donald, A. M. A Phase Diagram of the P3HT:PCBM Organic Photovoltaic System: Implications for Device Processing and Performance. *Macromolecules* **2011**, *44*, 2908–2917.
32. Li, L.; Tang, H.; Wu, H.; Lu, G.; Yang, X. Effects of Fullerene Solubility on the Crystallization of Poly(3-hexylthiophene) and Performance of Photovoltaic Devices. *Org. Electron.* **2009**, *10*, 1334–1344.
33. Yao, Y.; Hou, J.; Xu, Z.; Li, G.; Yang, Y. Effects of Solvent Mixtures on the Nanoscale Phase Separation in Polymer Solar Cells. *Adv. Funct. Mater.* **2008**, *18*, 1783–1789.
34. Flory, P. J. Thermodynamics of High Polymer Solutions. *J. Chem. Phys.* **1941**, *9*, 660–661.
35. van Krevelen, D. W. *Properties of Polymers: Their Correlation with Chemical Structure; Their Numerical Estimation and Prediction from Additive Group Contributions*; Elsevier: Amsterdam, The Netherlands, 2009.
36. Yang, X.; van Duren, J. K. J.; Rispens, M. T.; Hummelen, J. C.; Janssen, R. J. A.; Michels, M. A. J.; Loos, J. Crystalline Organization of a Methanofullerene as Used for Plastic Solar-Cell Applications. *Adv. Mater.* **2004**, *16*, 802–806.
37. Schmidt-Hansberg, B.; Baunach, M.; Krenn, J.; Walheim, S.; Lemmer, U.; Scharfer, P.; Schabel, W. Spatially Resolved Drying Kinetics of Multi-component Solution Cast Films for Organic Electronics. *Chem. Eng. Process.* **2011**, *50*, 509–515.
38. Sirringhaus, H.; Brown, P. J.; Friend, R. H.; Nielsen, M. M.; Bechgaard, K.; Langeveld-Voss, B. M. W.; Spiering, A. J. H.; Janssen, R. A. J.; Meijer, E. W.; Herwig, P.; *et al*. Two-Dimensional Charge Transport in Self-Organized, High-Mobility Conjugated Polymers. *Nature* **1999**, *401*, 685–688.
39. Kim, Y.; Cook, S.; Tuladhar, S. M.; Choulis, S. A.; Nelson, J.; Durrant, J. R.; Bradley, D. D. C.; Giles, M.; McCulloch, I.; Ha, C.-S.; *et al*. A Strong Regioregularity Effect in Self-Organizing Conjugated Polymer Films and High-Efficiency Polythiophene:Fullerene Solar Cells. *Nat. Mater.* **2006**, *5*, 197–203.
40. Sanyal, M.; Schmidt-Hansberg, B.; Klein, M. F. G.; Colsmann, A.; Munuera, C.; Vorobiev, A.; Lemmer, U.; Schabel, W.; Dosch, H.; Barrena, E. *In Situ* X-ray Study of Drying-Temperature Influence on the Structural Evolution of Bulk-Heterojunction Polymer–Fullerene Solar Cells Processed by Doctor-Blading. *Adv. Energy Mater.* **2011**, *1*, 363–367.
41. Chang, L.; Lademann, H. W. A.; Bonekamp, J. B.; Meerholz, K.; Moulé, A. J. Effect of Trace Solvent on the Morphology of P3HT:PCBM Bulk Heterojunction Solar Cells. *Adv. Funct. Mater.* **2011**, *21*, 1779–1787.
42. Wang, T.; Dunbar, A. D. F.; Staniec, P. A.; Pearson, A. J.; Hopkinson, P. E.; MacDonald, J. E.; Lilliu, S.; Pizzey, C.; Terrill, N. J.; Donald, A. M.; *et al*. The Development of Nanoscale Morphology in Polymer:Fullerene Photovoltaic Blends During Solvent Casting. *Soft Matter* **2010**, *6*, 4128–4134.
43. Yang, X.; van Duren, J. K. J.; Janssen, R. A. J.; Michels, M. A. J.; Loos, J. Morphology and Thermal Stability of the Active Layer in Poly(*p*-phenylenevinylene)/Methanofullerene Plastic Photovoltaic Devices. *Macromolecules* **2004**, *37*, 2151–2158.
44. Kim, J. S.; Ho, P. K. H.; Murphy, C. E.; Friend, R. H. Phase Separation in Polyfluorene-Based Conjugated Polymer Blends: Lateral and Vertical Analysis of Blend Spin-Cast Thin Films. *Macromolecules* **2004**, *37*, 2861–2871.
45. Koppe, M.; Scharber, M.; Brabec, C.; Duffy, W.; Heeney, M.; McCulloch, I. Polyterthiophenes as Donors for Polymer Solar Cells. *Adv. Funct. Mater.* **2007**, *17*, 1371–1376.
46. Collins, B. A.; Gann, E.; Guignard, L.; He, X.; McNeill, C. R.; Ade, H. Molecular Miscibility of Polymer–Fullerene Blends. *J. Phys. Chem. Lett.* **2010**, *1*, 3160–3166.
47. DeLongchamp, D. M.; Kline, R. J.; Fischer, D. A.; Richter, L. J.; Toney, M. F. Molecular Characterization of Organic Electronic Films. *Adv. Mater.* **2011**, *23*, 319–337.
48. Zeng, L.; Tang, C. W.; Chen, S. H. Effects of Active Layer Thickness and Thermal Annealing on Polythiophene: Fullerene Bulk Heterojunction Photovoltaic Devices. *Appl. Phys. Lett.* **2010**, *97*, 053305.
49. Heriot, S. Y.; Jones, R. A. L. An Interfacial Instability in a Transient Wetting Layer Leads to Lateral Phase Separation in Thin Spin-Cast Polymer-Blend Films. *Nat. Mater.* **2005**, *4*, 782–786.
50. Lee, H. K.; Jeon, J. H.; Wang, D. H.; Park, O. O.; Kim, J. K.; Im, S. H.; Park, J. H. Enhanced Charge Collection *via* Nanoporous Morphology in Polymer Solar Cells. *Appl. Phys. Lett.* **2010**, *96*, 103304.
51. Kopola, P.; Aernouts, T.; Guillerez, S.; Jin, H.; Tuomikoski, M.; Maaninen, A.; Hast, J. High Efficient Plastic Solar Cells Fabricated with a High-through-put Gravure Printing Method. *Sol. Energy Mater. Sol. Cells* **2010**, *94*, 1673–1680.
52. Boumann, M. M.; Havinge, E. E.; Janssen, R. A. J.; Meijer, E. W. Chiroptical Properties of Regioregular Chiral Polythiophenes. *Mol. Cryst. Liq. Cryst.* **1994**, *256*, 439–448.
53. Zhokhavets, U.; Erb, T.; Gobsch, G.; Al-Ibrahim, M.; Ambacher, O. Relation Between Absorption and Crystallinity of Poly(3-hexylthiophene)/Fullerene Films for Plastic Solar Cells. *Chem. Phys. Lett.* **2006**, *418*, 347–350.
54. Moulé, A. J.; Meerholz, K. Controlling Morphology in Polymer–Fullerene Mixtures. *Adv. Mater.* **2008**, *20*, 240–245.
55. Kim, J. H.; Park, J. H.; Lee, J. H.; Kim, J. S.; Sim, M.; Shima, C.; Cho, K. Bulk Heterojunction Solar Cells Based on Preformed Polythiophene Nanowires *via* Solubility-Induced Crystallization. *J. Mater. Chem.* **2010**, *20*, 7398–7405.
56. Berson, S.; DeBettignies, R.; Bailly, S.; Guillerez, S. Poly(3-hexylthiophene) Fibers for Photovoltaic Applications. *Adv. Funct. Mater.* **2007**, *17*, 1377–1384.